Inverse Modeling of the Initial Stage of the 1991 Pinatubo Volcanic Cloud Accounting for Radiative Feedback of Volcanic Ash

A. Ukhov[1], G. Stenchikov[1], S. Osipov[1], N. Krotkov[2], N. Gorkavyi[3], Can Li[4], O. Dubovik[5], and A. Lopatin[6]

[1]King Abdullah University of Science and Technology, Thuwal, Saudi Arabia
[2]NASA Goddard Space Flight Center, Greenbelt, MD, USA
[3]Science Systems and Applications, Lanham, MD, USA
[4]University of Maryland, College Park, MD, USA
[5]Univ. Lille, CNRS, UMR 8518 - LOA - Laboratoire d'Optique Atmosphefique, Lille, France
[6]GRASP SAS, Remote Sensing Developments, 59260 Lezennes, France

Key Points:

- Pinatubo erupted 10.4 Mt (of the total 15.5 Mt) of SO_2 and 29.3 Mt (of the total 66.5 Mt) of fine ash in the stratosphere.
- AOD develops faster than observed due to significant tropospheric emission of SO_2 that quickly converts to sulfate aerosol.
- Accounting for ash radiative heating improves inverse modeling results.

Keywords: Pinatubo, TOMS, UV aerosol index, SO_2, ash, inverse modeling, radiative transfer, WRF-Chem, DISORT

Corresponding author: Alexander Ukhov, alexander.ukhov@kaust.edu.sa

Abstract

The way volcanic clouds evolve is very sensitive to the initial spatial 3D distributions of volcanic materials, which are often unknown. In this study, we conducted inverse modeling of the Mt. Pinatubo cloud using TOMS 2D mapping of Aerosol Index and SO_2 loading during the first three post-eruption days to estimate the time-dependent emissions profiles and initial 3D spatial distributions of volcanic ash and SO_2. We account for aerosol radiative feedback and dynamic lofting of volcanic ash in the inversion calculations for the first time. This resulted in a lower ash injection height (by 1.5 km for ash) than without ash radiative feedback. The Pinatubo eruption ejected ≈77% of fine ash at 12 to 23 km, ≈65% of SO_2 at 18 to 25 km. In contrast with previous studies, which suggested that all volcanic materials were emitted above the tropopause, a significant fraction of SO_2 (5.1 of 15.5 Mt) and fine ash (37.2 of 66.5 Mt) were ejected in the troposphere, where SO_2 quickly oxidized into sulfate aerosol that is short-lived in the troposphere. This explains the early presence of sulfate aerosols in the plume and why the models can reproduce the observed volcanic aerosols' optical depth (AOD), assuming lower-than-observed SO_2 emission in the stratosphere. Despite the quicker than in observations build-up of sulfate AOD, in a month after the eruption, the evolution of the Pinatubo AOD simulated using the obtained ash and SO_2 initial distributions converges with the available stratospheric aerosol and gas experiment (SAGE) observations.

Plain Language Summary

The total ozone mapping spectrometer (TOMS) instrument observed the initial 2D distributions of the aerosol index and SO_2 column loadings from the largest eruption in the twentieth century, the 1991 Mt. Pinatubo eruption. However, the ash and SO_2 vertical profiles could not be directly obtained from these observations. Thus, we conduct inverse modeling of the Mt. Pinatubo cloud observed during the first three post-eruption days to estimate the time-dependent emissions profiles and initial 3D spatial distributions of volcanic ash and SO_2. For the forward simulations, we use a regional meteorological chemical transport model accounting for aerosol radiative feedback. Obtained initial 3D distributions of volcanic materials are sufficient to initiate volcanic cloud forecasts and the climate model simulations of volcanic effects. The proposed methodology can be used for reconstructing vertical profiles of the emitted aerosols and gases in a wide range of volcanic eruptions and pyroconvection events.

1 Introduction

Volcanic eruptions inject ash, SO_2, halogens, water vapor, and other volcanic material into the atmosphere. Weak volcanic activity typically releases trace gases and ash particles within the troposphere, where they are short-lived. Strong volcanic explosions can overshoot the tropopause (TP) and deliver volcanic materials to the stratosphere, which last for a few years and causes long-term climatic impacts (Robock, 2000; Osipov et al., 2020; English et al., 2013; Timmreck et al., 2012; Stenchikov, 2021; Ramaswamy et al., 2019).

The long-term evolution of stratospheric volcanic clouds is sensitive to the height of emissions. The vertical distribution of volcanic material shapes the intense dynamic, chemical, and microphysical processes in a volcanic cloud (Stenchikov, 2021; Abdelkader et al., 2022). The satellite observations available at the time of the Mt. Pinatubo eruption in 1991 lack the vertically resolved information on the early volcanic plume but provide column-integrated characteristics, such as the SO_2 column loading (Bluth et al., 1992; Guo, Bluth, et al., 2004; A. J. Krueger, 1983; A. Krueger et al., 1995) and aerosol index (AI) (Herman et al., 1997; Seftor et al., 1997; Torres et al., 1998; Krotkov et al., 1999).

To simulate the climate effects of volcanic eruptions within the latest general circulation models, the initial distributions of eruptive materials must be prescribed based on observations, or the complex volcanic emission process must be parameterized, assuming that the estimated mass of volcanic materials is emitted in a particular volume with predefined emission rates (Stunder et al., 2007; Stenchikov et al., 2021; Stuefer et al., 2013; Suzuki et al., 1983). The initial vertical distribution of volcanic materials remains an issue that adds uncertainty to the volcanic impact modeling.

To improve the initial vertical distributions of the eruptive materials, Fero et al. (2009), S. A. Carn et al. (2009), and Prata et al. (2007) applied the trial-and-error approach using transport and dispersion models. For example, Fero et al. (2009) conducted over 500 simulations of ash transport in the aftermath of the Mt. Pinatubo eruption using the PUFF model (Searcy et al., 1998), varying the initial ash distributions to fit the observations. They concluded that ash was predominantly released and advected at the TP altitude of ≈17 km. For the reasons mentioned at the beginning, information on the vertical distribution of SO_2 emissions from the 1991 Mt. Pinatubo eruption is of interest, but, unfortunately, is still uncertain. For example, in Quaglia et al. (2023), six global models were initialized by varying the SO_2 injection amount (ranging between 5 and 10 Tg S) and the altitude of injection (between 18–25 km).

Inverse modeling is considered more efficient and versatile in obtaining optimal initial conditions than the trial-and-error approach. Seibert (2000), Eckhardt et al. (2008), Kristiansen et al. (2010), Stohl et al. (2011), and Seibert et al. (2011) used an inversion algorithm to obtain the vertical distribution of volcanic emissions. They employed an off-line transport model, FLEXPART (Stohl et al., 2005), driven by wind fields from numerical weather prediction models. Such settings do not account for the radiative feedback of aerosols. For small volcanic eruptions, the feedback is usually weak and can be ignored. For larger volcanic eruptions with a volcanic explosivity index (VEI) > 5, such as the 1991 Mt. Pinatubo eruption (VEI $= 6$), ash radiative heating alters the atmospheric flow and lifts the volcanic cloud. The radiative effect of ash is especially pronounced during the first few post-eruption days (Niemeier et al., 2009; Stenchikov et al., 2021).

In this study, we present the inverse modeling of ash and SO_2 clouds for the 1991 Mt. Pinatubo eruption for the first time accounting for the radiative feedback of ash. We focus on the following research questions:

- What were the 3D initial distributions of volcanic SO_2 and ash in the first days after the 1991 Mt. Pinatubo eruption?
- How are ash and SO_2 emissions partitioned across the TP?
- What are the effects of ash radiative feedback on volcanic plume evolution and the inverted emission profiles of ash and SO_2?

2 Inversion

By conducting inverse modeling, we calculate the vertical and temporal distributions of the mass emission rates of ash and SO_2, providing the best least square fit between the observed and modeled 2D ash and SO_2 column loadings. The procedure calculates the 3D distributions of ash and SO_2 for the first few days after the eruption. The SO_2 radiative feedback is relatively low for a Pinatubo-size eruption (Stenchikov et al., 2021), and we neglect it, but the radiative feedback of ash is accounted for. Therefore, we split the inversion of SO_2 and ash distributions. In the first step, we perform the inversion of ash emissions, and in the second step, we invert the SO_2 emissions, using the inverted distributions of ash emissions.

2.1 Observations

The cloud of eruptive material ejected by the Mt. Pinatubo eruption was observed by several remote sensing instruments, including the total ozone mapping spectrometer (TOMS) (Guo, Bluth, et al., 2004), advanced very high-resolution radiometer (AVHRR) (Long & Stowe, 1994), and stratospheric aerosol and gas experiment (SAGE) (L. W. Thomason, 1992). The TOMS retrievals provide 2D maps of the AI and SO_2 column loading and estimated the total mass of the emitted SO_2 to reach ≈12 to 17 Mt (Bluth et al., 1992; A. Krueger et al., 1995; Krotkov et al., 1997; Seftor et al., 1997; Torres et al., 1998; Krotkov et al., 1999; Guo, Bluth, et al., 2004; Fisher et al., 2019). According to the AVHRR, the mass of fine ash reached 75 to 80 Mt. Holasek et al. (1996) described the height of the volcanic cloud during the entire eruptive activity period, which acts as an upper limit for the altitude of the erupted material.

We use TOMS retrievals (Fisher et al., 2019) as input for the inversion (see Fig. 1). The TOMS instrument was aboard the Nimbus-7, a sun-synchronous polar orbiting satellite, and passed over the Mt. Pinatubo ash cloud once a day. Soon after the eruption, the TOMS detected high levels of SO_2 loading and positive AI values, indicating the presence of absorbing volcanic ash (Seftor et al., 1997; Bluth et al., 1992; Torres et al., 1998; Krotkov et al., 1999; A. Krueger et al., 1995). Figure 1a illustrates that the ash cloud dispersed quickly and was hardly detectable on 17 and 18 June (Self et al., 1993). Thus, for the inversion, we use only a single-day observation made at 0345 UTC on 16 June.

The AI indicates the presence of UV-absorbing aerosols (e.g., silicate ash or soot) but cannot be, in the general case, easily converted into aerosol mass. However, the AI and aerosol optical depth (AOD) are linearly related if the volcanic cloud is relatively thin (i.e., ash AOD < 5) (Krotkov et al., 1999). Given that the AOD is proportional to the loading, we can assume the linear relationship between the AI and ash loading. Therefore, we derived the ash loading by scaling the AI field on 16 June, assuming that the mass of emitted fine ash is 75 Mt. See Sec. 2.2 for details. We use these synthetic loadings in the inversion procedure and test their validity in Sec. 4.

According to the TOMS retrieval, the daily amounts of SO_2 in the volcanic cloud were 8.8, 12.0, and 11.0 Mt on 16, 17, and 18 June, respectively (see Fig. 1b). The SO_2 mass on 16 June is smaller than on 17 June, and the SO_2 mass increase cannot be explained within the current modeling framework. Therefore we do not use SO_2 observation on 16 June, and following Guo, Bluth, et al. (2004) scale TOMS SO_2 column loadings (Krotkov et al., 2019) by a factor = 1.42, assuming that 17 Mt was observed on 17 June.

2.2 Emissions

The altitude of the erupted volcanic plume depends on the vertical extent of the eruptive jet (or the overshooting height of the co-ignimbrite convection) and subsequent lofting caused by radiative heating of the ash cloud. The ash emission height should not exceed the observed plume height but could be lower. Therefore, we choose the top of a priori emission profiles to fit the heights of the plume in Figure 1 in Holasek et al. (1996). The bottom boundary of the emissions is set to 9 km. We initiate emissions on 15 June at 0141 UTC and stop at 1541 UTC, right after the climactic phase of the eruption is finished (Holasek et al., 1996) (see Fig. 2).

Guo, Rose, et al. (2004) estimated that the eruption of Mt. Pinatubo in 1991 ejected 80 Mt (50% uncertainty) of fine ash. We follow Stenchikov et al. (2021) and assume that Mt. Pinatubo injected 100 Mt of fine ash with a log-normal size distribution, which has a median radius of 2.4 μm and the geometric standard deviation of 1.8 (Niemeier et al., 2009). The aerosol scheme, which we use in the forward model, accounts only for particles with radii <10 μm. Therefore, the large-radius tail of this distribution is neglected,

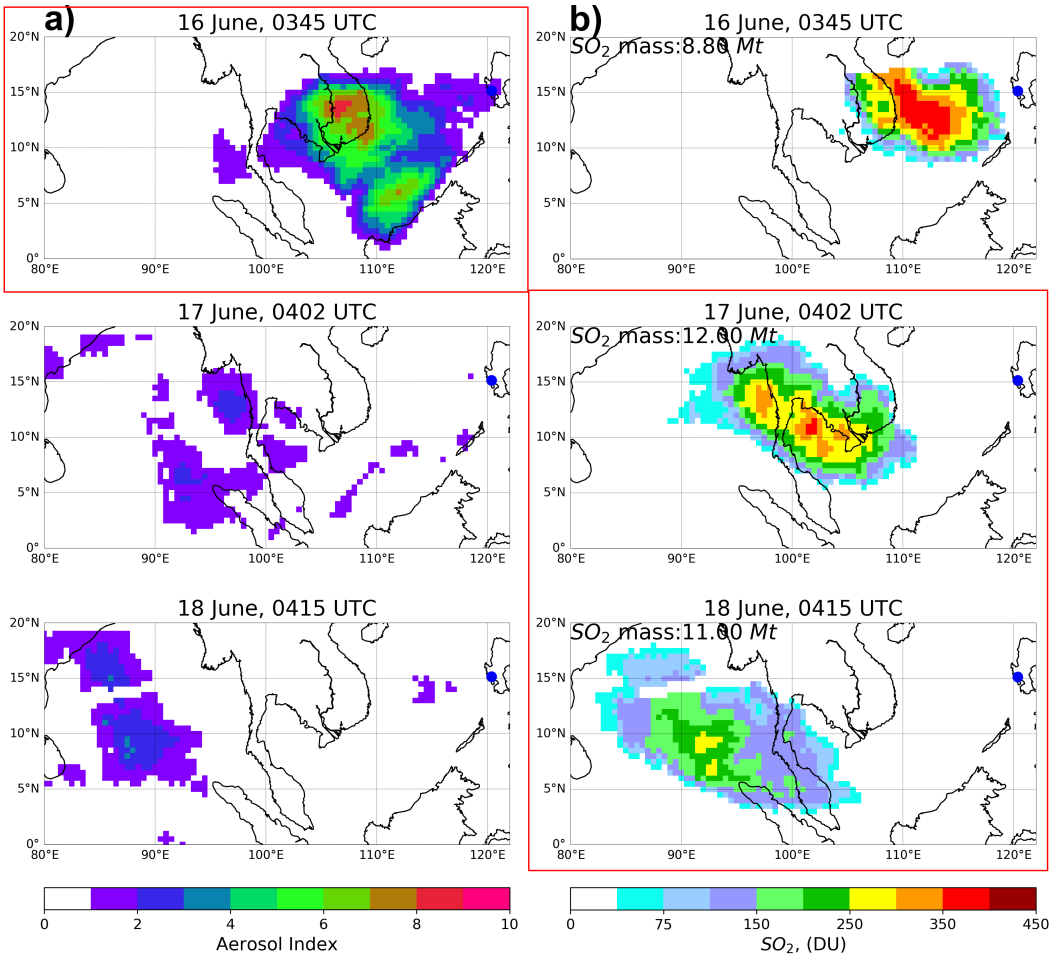

Figure 1. TOMS retrievals of a) AI, b) column loadings (DU) and total mass of SO_2 (Mt), 8.8 Mt on 16 June at 0345 UTC, 12.0 Mt on 17 June at 0402 UTC, and 11 Mt on 18 June at 0415 UTC. Data are presented on a $0.5^\circ \times 0.5^\circ$ latitude-longitude grid. The red panels highlight the temporal sampling of AI and SO_2 used in the inverse calculations; 1 DU = 2.687×10^{20} (molecules m^{-2}).

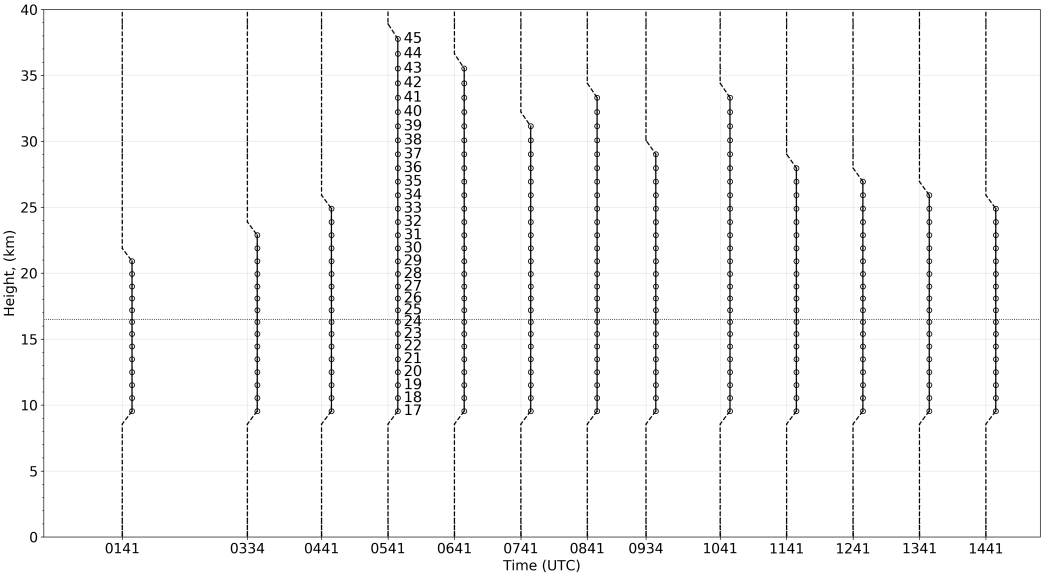

Figure 2. A priori emission profiles. Each circle represents an individual emission pulse out of 269 pulses. Numbers correspond to the model level. The dotted horizontal line represents the tropopause.

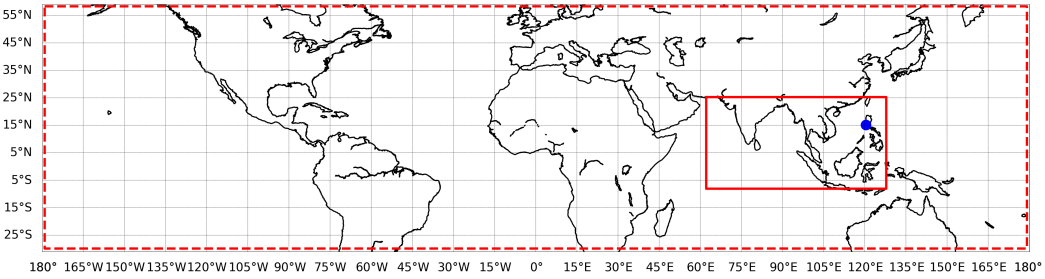

Figure 3. Modeling domains. Solid red lines outline the domain for inversion modeling. Dashed red lines outline the modeling domain used in a three-month run to study the long-term evolution of the volcanic cloud based on the prescribed ash and SO_2 initial conditions. The blue dot marks the location of Mt. Pinatubo.

assuming that particles with radii > 10 μm are short-lived due to gravitational settling. The remaining mass of emitted fine ash with radii <10 μm is 75 Mt, close to that suggested by Guo, Rose, et al. (2004). The total emitted SO_2 mass is 17 Mt (Bluth et al., 1992; Guo, Bluth, et al., 2004; Stenchikov et al., 2021).

2.3 Forward Modeling

We employ the Weather Research Forecasting Model coupled with the aerosol-chemistry module (WRF-Chem v3.7.1) (Grell et al., 2005; Skamarock et al., 2005) as a forward model. In contrast with the previous inverse studies, the radiative heating of volcanic ash is included in the calculations. The simulation domain (60°E - 130°E; 7°S–25°N) for inversion is centered at 9°N, 95°E, has 54×74×39 grid cells (altitude, longitude, and latitude, respectively) and 100×100 km resolution (see Fig. 3). The simulation domain for the three-

month run spans across the 30°S - 60°N latitude belt and has the same horizontal and vertical resolution as the smaller domain.

To model atmospheric chemistry, we employed the Regional Atmospheric Chemistry Mechanism (RACM) (Stockwell et al., 1997) containing 77 chemical species and 237 chemical reactions, including 23 photochemical reactions. An online computation of the photolysis rates for the 23 photochemical reactions of the RACM gas-phase chemical mechanism is implemented according to Madronich (1987). The Georgia Tech/Goddard Global Ozone Chemistry Aerosol Radiation and Transport (GOCART) aerosol and chemistry module (Chin et al., 2002) is used to calculate the SO_2 to sulfate (SO_4) oxidation by the hydroxyl radical OH whose abundance is simulated by RACM.

We employed the GOCART aerosol scheme to simulate volcanic ash. Five bins with radius edges of 0.1, 1.0, 1.8, 3.0, 6.0, and 10 μm approximate the ash size distribution. The ash density is assumed to be 2500 kgm^{-3} for the first bin and 2650 kgm^{-3} for the second to fifth bins. We assume the same size distribution of the emitted ash as that in (Niemeier et al., 2009; Stenchikov et al., 2021) and allocate 0.1%, 1.5%, 9.5%, 45%, and 43.9% of the mass to ash bins 1 to 5, respectively. The complex refractive index (RI) of the ash is set to 1.55+i0.001 in the shortwave spectral range (Pollack et al., 1973; S. Carn & Krotkov, 2016). The larger imaginary part of the RI corresponds to the stronger absorption of solar radiation, enhancing atmospheric heating. The gravitational settling of ash in WRF-Chem was improved following Ukhov et al. (2021). The terminal settling velocity of ash particles is calculated for the mean radii within each bin.

Spectral nudging (Miguez-Macho et al., 2004) has been applied above the PBL (>5.0 km) to horizontal wind components (u and v) for the European Centre for Medium-Range Weather Forecasts Era-interim reanalysis fields. The nudging coefficient equals 0.0001 s^{-1}. Only wavelengths larger than 450 km are nudged. This setting allows accounting for the realistic phase of QBO and keeps the large-scale motions close to the observations, letting the model develop small-scale disturbances freely.

The meteorological initial and boundary conditions for WRF-Chem are also calculated using the ERA-Interim reanalysis product (Dee et al., 2011). The ERA-Interim reanalysis data were obtained with a 0.75° × 0.75° horizontal and 6-h temporal resolution.

2.4 Inverse Modeling

We define the a priori emission vectors e (Mt sec^{-1}) for ash and SO_2 and discretize emission profiles into the series of n pulses (in this case, $n = 269$). Each pulse is characterized by the height of ejection, mass emission rate e_i, start time, and duration Δt_i (s), where $1 \leq i \leq n$. The duration Δt_i is ≈2 h for the first 12 pulses ($0 \leq i \leq 12$) and equals ≈1 h for other pulses. We assume that the step-wise emission pulses are distributed from 9 km to the observed top of the volcanic plume (Holasek et al., 1996) (Fig. 2).

The ith model run maps the ith emission pulse into the 2D observation space of column loadings. Each pulse is simulated separately using one WRF-Chem model run to obtain the receptor vector u_i (μg m^{-2}) with dimension ($m \times 1$), where m is the number of grid cells in the domain (in this case $m = 74 \times 39 = 2886$). The combination of n receptor vectors u_i provides the source-receptor matrix M with the dimensions ($m \times n$).

Each WRF-Chem run also simulates the full-fledged "background" volcanic eruption according to a priori emission profiles, along with the simulation of the individual emission pulse to account for the radiative heating of ash on dynamics. The mass emission rate e_i of each emission pulse is distributed between five radiatively inactive tracers subjected to gravitational settling. The "background" eruption is simulated using

five ash bins from the GOCART aerosol scheme. Thus, the dispersion of tracers is affected by heating the ash from the "background" eruption. The size, density, and tracer mass distribution within the emission pulse corresponds to the five ash bins mentioned in Sec. 2.3.

The linear combination of emissions $\sum_{i=1}^{n} c_i e_i \Delta t_i$ (c_i denotes the components of the dimensionless scaling vector c $(n \times 1)$) generates a receptor vector $u = Mc$, or in the component form:

$$u^k = \sum_{i=1}^{n} c_i u_i^k \tag{1}$$

where u^k and u_i^k represent k components of vectors u and u_i, $1 \leq k \leq m$. In addition, u_i^k is the response (expressed in terms of the column loading) to the ith emission pulse in the kth grid cell of the computational domain. The response vector u is evaluated against observations represented by the vector y_o (μg m^{-2}). Both vectors have the same dimension $(m \times 1)$.

We aim to determine the scaling vector c that minimizes the cost function $J = J_1 + J_2$. Further, J_1 is the misfit between the modeled values and observations y_o^k in the kth grid cell, and J_2 is the deviation from the a priori nondimensional scaling vector c^a with dimensions $(n \times 1)$:

$$J_1 = \sum_{k=1}^{m} \left(\sum_{i=1}^{n} c_i u_i^k - y_o^k \right)^2, \tag{2}$$

$$J_2 = \beta \sum_{i=1}^{n} \left(c_i - c_i^a \right)^2, \tag{3}$$

where J_2 regularizes the solution by nudging vector c to the vector c^a from the previous iteration. The regularization parameter $\beta \geq 0$ (μg^2 m^{-4}) determines the strength of this nudging. Moreover, β is chosen experimentally to provide computational stability without over-smoothing the solution. A minimum of J provides the following system of n linear equations:

$$\sum_{i=1}^{n} a_{ij} c_i + \beta c_j - \sum_{k=1}^{m} y_o^k u_j^k - \beta c_j^a = 0, \tag{4}$$

where $1 \leq i, j \leq n$ and $a_{ij} = \sum_{k=1}^{m} u_i^k u_j^k$ are elements of the Gram matrix with dimension $(n \times n)$. The β value must be of the order of diagonal elements of this matrix to make the regularization effective. Rearranging (4) provides the following equation:

$$\sum_{i,j=1}^{n} \tilde{a}_{ij} c_i = \sum_{k=1}^{m} y_o^k u_j^k + \beta c_j^a, \tag{5}$$

where $\tilde{a}_{ij} = a_{ij}$, if $i \neq j$ and $\tilde{a}_{jj} = a_{jj} + \beta$, if $i = j$. Equation (5) could also be written in matrix form:

$$\tilde{A} \cdot c = y_o \cdot u + \beta c^a, \tag{6}$$

where $\tilde{\mathrm{A}}$ is a matrix built from elements $\tilde{\mathrm{a}}_{ij}$ (i.e., $\tilde{\mathrm{A}} = (\tilde{\mathrm{a}}_{ij})$).

We solve this system iteratively until vectors c and c^a converge. At the first iteration, $c_i^a = 1$, and e_i is equal for each pulse and is chosen so that $\sum_{i=1}^{n} c_i^a e_i \Delta t_i$ equals the a priori total mass of the eruptive material. At the next iteration, we recalculate the components of vector e as $e_i \cdot c_i$ and redefine vector c^a using vector c from the previous iteration. Emissions should be positive; thus, we overwrite the negative c_i with $0.001 \cdot max(c)$ and the corresponding e_i with $0.001 \cdot e_i \cdot max(c)$.

The available observations of AI and SO_2 column loadings are interpolated on the WRF-Chem horizontal grid, saving the surface integral. We use the fractional skill score (FSS) developed by Roberts and Lean (2008), the Pearson correlation coefficient (R), and the relative root mean squared error ($RRMSE$; see Appendix A) to evaluate how well the iterations converge to the quasi-optimal solution.

3 Derivation of Emission Profiles and 3D Distributions of Eruptive Materials

First, we derive the emission profiles of ash because ash is the primary heating agent and drives the lofting of the volcanic material. Once the ash emission profiles are determined, they are used in the inversion procedure for SO_2. The same inversion procedure of ash and SO_2 profiles was repeated with the radiative feedback disabled to demonstrate the effect of the radiative heating of the ash cloud. The nomenclature for all WRF-Chem runs is presented in Table 1.

Description	Begin and end dates, UTC	Ash radiative feedback
Ash emission inversion runs		
The **ASH_SOL_RAD** run is based on the inverted ash emission profile obtained on the fourth iteration. The AI field is scaled to 75 Mt. During every iteration, each emission pulse emits volcanic ash and tracers. The first iteration emitted 75 Mt of ash and tracers. A priori emission profiles are presented in Figure 2.	0000 15 June, 0400 16 June	Yes
The **ASH_SOL_NO_RAD** run is similar to ASH_SOL_RAD, but the radiative feedback of ash is disabled, and only tracers are emitted.	0000 15 June, 0400 16 June	No
SO_2 emission inversion runs		
The **SO2_SOL_RAD** run is based on the inverted SO_2 emission profile obtained on the fourth iteration. A priori emissions are scaled to 17 Mt of SO_2. The observed SO_2 column loadings employed in the inversion were scaled to produce 17 Mt at 0402 UTC on 17 June. A priori emission profiles are presented in Figure 2. The ash emission profile is according to the ASH_SOL_RAD run.	0000 15 June, 0400 18 June	Yes
The **SO2_SOL_NO_RAD** run is similar to SO2_SOL_RAD, but the radiative feedback of ash is disabled. Ash is emitted according to the profile in the ASH_SOL_NO_RAD run.	0000 15 June, 0400 18 June	No
Three-month runs in latitude belt		
The **SOL_RAD** run derives the initial conditions of the ash, SO_2, and sulfate aerosol from SO2_SOL_RAD run at 0400 UTC on 16 June.	0400 16 June, 0000 15 Sep	Yes
The **CW17S111A10** run from Stenchikov et al. (2021) with the prescribed 17 Mt of SO_2 and 75 Mt of fine ash emissions during 24 h in the $300\times100\times4$ km^3 region according to parabolic emission profile centered at 17 km in height with boundaries at 15 and 19 km.	0000 15 June, 0000 15 Sep	Yes

Table 1. Nomenclature of WRF-Chem runs. Run abbreviations are highlighted in bold.

3.1 Ash

In the first iteration, we use the emission profile in Fig. 2 for the ash-tracer and background ash. The total ash mass emitted by all pulses and the background ash emission is 75 Mt each. In both cases, the e_i emission pulses are equal, and c_i =1. We choose $\beta = 10^{14}$ ($\mu g^2 m^{-4}$) and conducted four iterations as described in Sec. 2.4. In the next iteration, the inverted ash emission profiles and scaling vector c obtained on the previous iteration are used as a priori emission profiles and vector c^a. In each iteration, we recalculate the source-receptor matrix M. To quantify the effect of the ash radiative feedback, we also conduct inverse modeling with the radiative feedback turned off. In this case, we do not recalculate the source-receptor matrix M, as the atmospheric flow is not affected due to the absence of ash radiative heating. The ash emission profiles obtained after the fourth iteration in the ASH_SOL_RAD and ASH_SOL_NO_RAD runs are presented in Fig. 4.

The total erupted mass of the ash obtained in the ASH_SOL_RAD run equals 66.53 Mt and is 62.67 Mt in the ASH_SOL_NO_RAD run. Ash emissions are most intensive during the time interval 1041–1241 UTC in both runs. The most ash mass is released just below the TP level (assumed at 16.5 km), although some ash was ejected above 25 km. The corresponding time-integrated emission profiles demonstrate that, in the ASH_SOL_RAD run, the two altitudes of the maximum ash mass release are about 1.5 km below the corresponding levels, where the maximum ash mass is released in the ASH_SOL_NO_RAD run (i.e., without plume lofting; see Fig. 4b,c). In the ASH_SOL_RAD run, ≈10% of ash is emitted above 25 km, whereas in the ASH_SOL_NO_RAD run, only 3.5%. For both profiles, ≈34% to 44% of ash mass is emitted above TP, 77% to 80% of ash mass is within the 12- to 23-km layer, and about 56% to 66% of ash is ejected into the troposphere.

Figure 5 compares ash column loadings obtained from the ASH_SOL_RAD and ASH_SOL_NO_RAD runs, normalized with a 75 Mt AI field, latitude-averaged (5°–15°N) vertical cross sections of ash mass concentrations, and maps of the total AOD at 550 nm at 0400 UTC on 16 June. The spatial patterns of the ash column loadings are similar in both runs, repeating the 2D structure of the observed AI field. However, the statistical scores FSS, R, and $RRMSE$ computed with respect to observations are better in the ASH_SOL_RAD run than in the ASH_SOL_NO_RAD run. In both runs, the secondary maximum of the AI at 8°N, 113°E is captured, although it was not present in the first iterations (not shown). The latitude-averaged vertical cross sections of ash mass concentrations are slightly different (Fig. 5c,f) being displaced vertically by about 1.5 km, which is consistent with the finding that during the first days, the Pinatubo volcanic cloud was lofted by about 1 km per day (Stenchikov et al., 2021). The ash optical depth in Fig. 5d,g repeats the shape of the ash loading distribution (as expected) and is of the order of 4, reaching 6 to 8 in some areas.

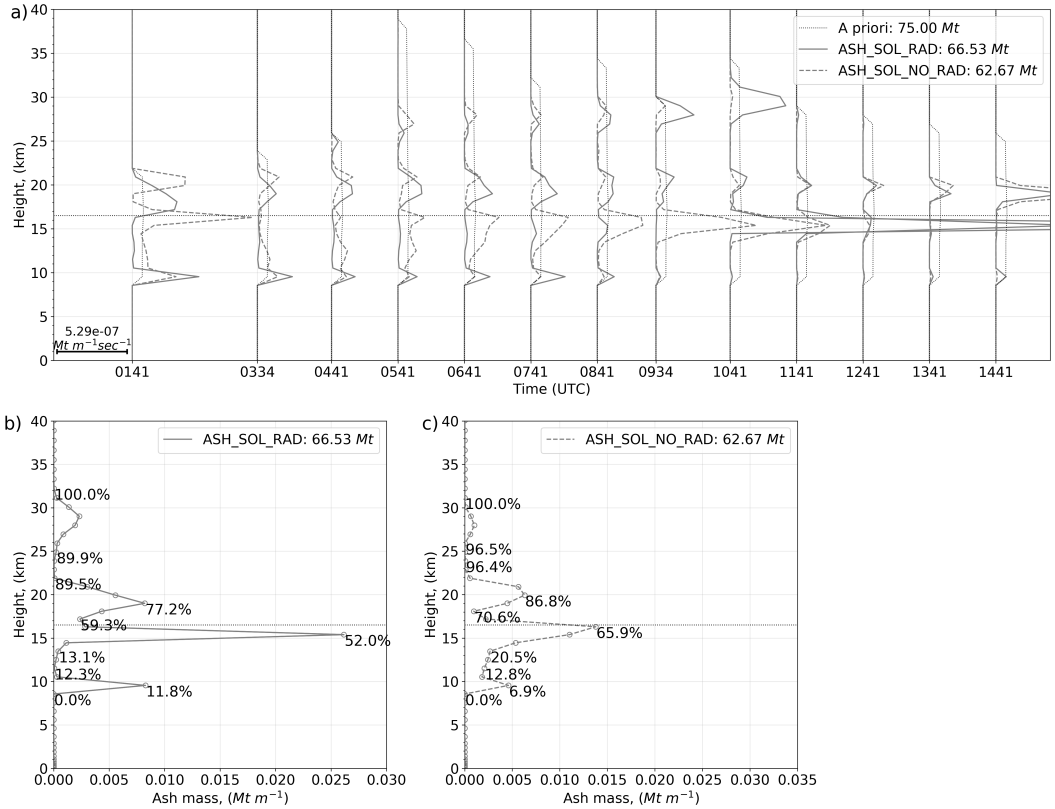

Figure 4. Ash emission profiles: a) a posteriori ash emission profiles ($Mt\ m^{-1}s^{-1}$) from the ASH_SOL_RAD (solid line), ASH_SOL_NO_RAD (dashed line), and a priori (dotted line) runs. Corresponding a posteriori time-integrated ash emission profiles ($Mt\ m^{-1}$) from the b) ASH_SOL_RAD and c) ASH_SOL_NO_RAD runs. Percentage numbers on plots b) and c) denote vertically integrated from bottom to top ash emission mass. The dotted horizontal line marks the tropopause.

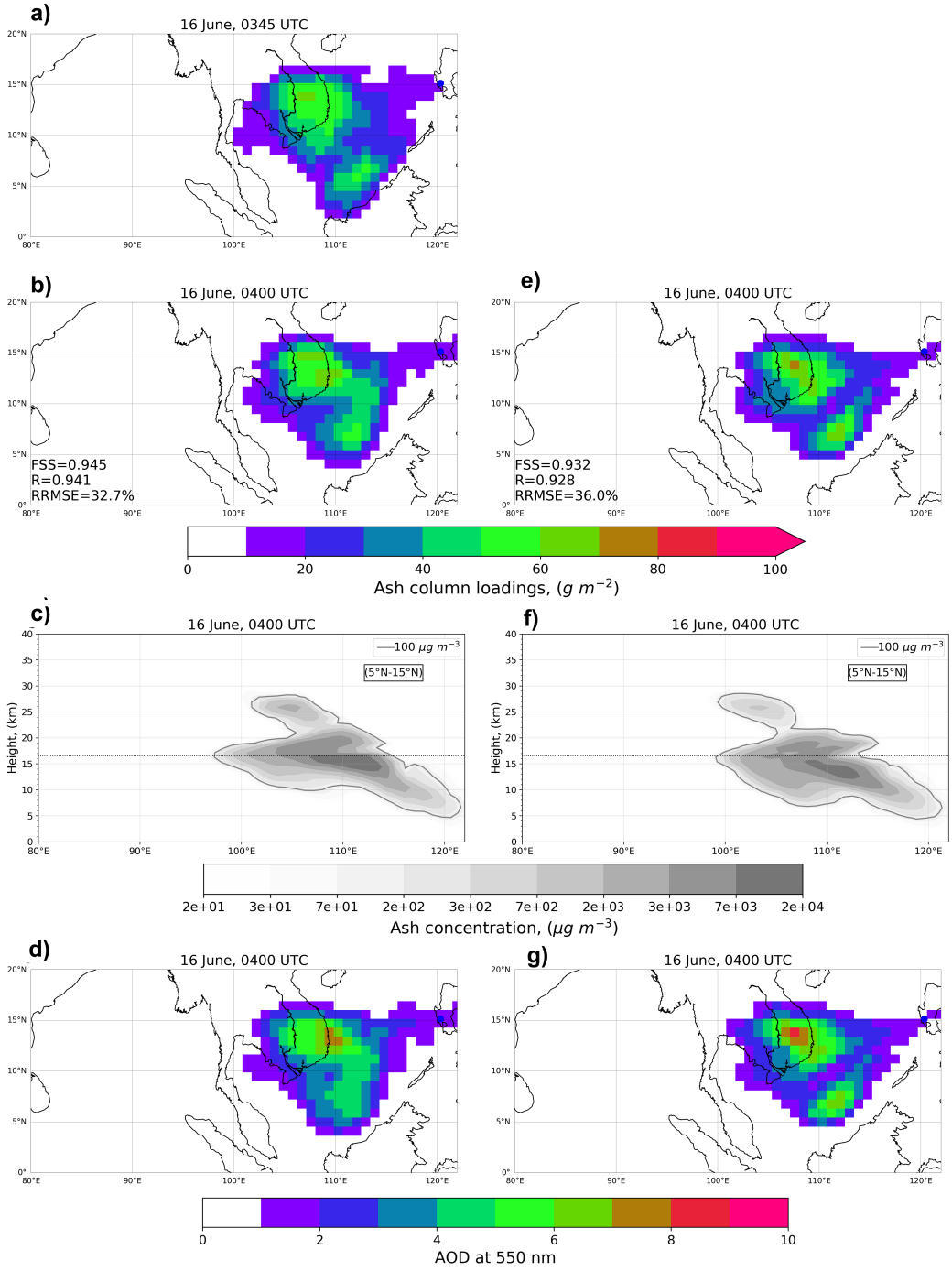

Figure 5. Observed on 16 June at 0345 UTC and simulated aerosol diagnostics on 16 June at 0400 UTC. a) TOMS AI normalized by 75 Mt. Diagnostics from the ASH_SOL_RAD run: b) simulated ash column loadings, c) cross section of latitude-averaged (5°–15°N) ash mass concentrations (μg m^{-3}), d) column AOD at 550 nm. e, f, g) same diagnostics from the ASH_SOL_NO_RAD run. The dotted horizontal line on c) and f) indicates the tropopause.

3.2 SO_2

We employ the TOMS retrievals of the SO_2 column loadings on 17 and 18 June. In this case, the dimensions of the observation vector y_o, vectors u_i, and vertical dimensions of matrix M equal $2\times m$. We disregard the observations on 16 June because they display about half of the expected SO_2 emission mass. This outcome is either because of missing data due to instrumental saturation or is a result of an unaccounted physics (e.g., SO_2 uptake by ash (Zhu et al., 2020), or release of SO_2 from ice crystals (Guo, Bluth, et al., 2004)), or ash and early sulfate interference (Fisher et al., 2019). The SO_2 emissions are set the same way as for ash (see Fig. 2). We scaled the n-dimensional emission rate vector e so that the total a priori SO_2 emission equals 17 Mt on 17 June. The a posteriori ash emission profiles obtained in the ASH_SOL_RAD run are used in the SO2_SOL_RAD run to account for the "background" ash radiative heating. We choose $\beta = 10^{13}$ ($\mu g^2 m^{-4}$) and conducted four iterations.

The a posteriori SO_2 emission profiles obtained in the SO2_SOL_RAD and SO2_SOL_NO_RAD runs are depicted in Fig. 6. The masses of ejected SO_2 are 15.54 and 16.73 Mt for the experiments with and without aerosol radiative feedback, respectively. The vertical and temporal distributions of the emissions in these two experiments are somewhat different, but the emissions profiles integrated over time are qualitatively similar (see Fig. 6b,c). In both experiments, most of the SO_2 is released at ≈20 km, and there are no emissions above 26 km. In the SO2_SOL_RAD run, 67% of SO_2 is emitted above the TP, but in the SO2_SOL_NO_RAD run, 55.5% of the SO_2 mass is distributed in three stratospheric layers with the peaks at 20, 22 and 24 km. In the SO2_SOL_RAD run, 65% of the SO_2 was emitted between 18 and 25 km with a maximum mass ejected at ≈20 km.

The previous studies assumed that all SO_2 was injected in the stratosphere (Niemeier et al., 2009; Brühl et al., 2018; Aquila et al., 2012; Stenchikov et al., 2021; A. Krueger et al., 1995; Guo, Bluth, et al., 2004; Bluth et al., 1992), but the a posteriori integrated profiles reveal that a significant amount of SO_2 is released into the troposphere: 33% in SO2_SOL_RAD and 44.5% in SO2_SOL_NO_RAD (see Fig. 6b,c). TOMS evaluates the SO_2 column density and mass assuming Gaussian vertical profile shape, with the center of mass altitude equal 18 km and 2 km standard deviation (Fisher et al., 2019; Krotkov et al., 2019). The fate of the tropospheric and stratospheric SO_2 is different, i.e. most tropospheric SO_2 converts into sulfate within a few days. Therefore, we can conclude that no more than 70% of the emitted SO_2 converts to stratospheric aerosols.

The time evolution of the emitted ash and SO_2 in the SO2_SOL_RAD run and decomposition on tropospheric and stratospheric emissions is presented in Fig. 7. The figure illustrates two strong ash emissions peaks. One at the very beginning of the eruption, the second between 1041 and 1141 UTC. The SO_2 emissions are gradually increasing from the beginning until 1041 UTC and between 1241 and 1541 UTC.

Figure 8 compares the SO_2 column loadings from the SO2_SOL_RAD, and SO2_SOL_NO_RAD runs with the TOMS retrievals. We also determine the mass of SO_2 below and above TP. We do not use the TOMS SO_2 observations on 16 June for inversion calculations but retain them for illustration purposes. We display TOMS retrievals scaled by a factor of 1.42 to obtain 17 Mt on 17 June, as discussed in Sec. 2.1. In the SO2_SOL_RAD experiment, the mass of SO_2 above the TP increases due to the lofting of the tropospheric SO_2, whereas the mass of SO_2 below the TP decreases relatively quickly due to the conversion to sulfate aerosols. During the 16-18 June period, the amount of SO_2 above the TP grows more rapidly in the SO2_SOL_RAD run in comparison with SO2_SOL_NO_RAD run (1.4 Mt versus 0.3 Mt, respectively) due to radiative heating and lofting. The statistical scores FSS, R, and $RRMSE$ are computed with respect to TOMS SO_2 retrievals for 17 and 18 June and are better for the SO2_SOL_RAD run than for the SO2_SOL_NO_RAD.

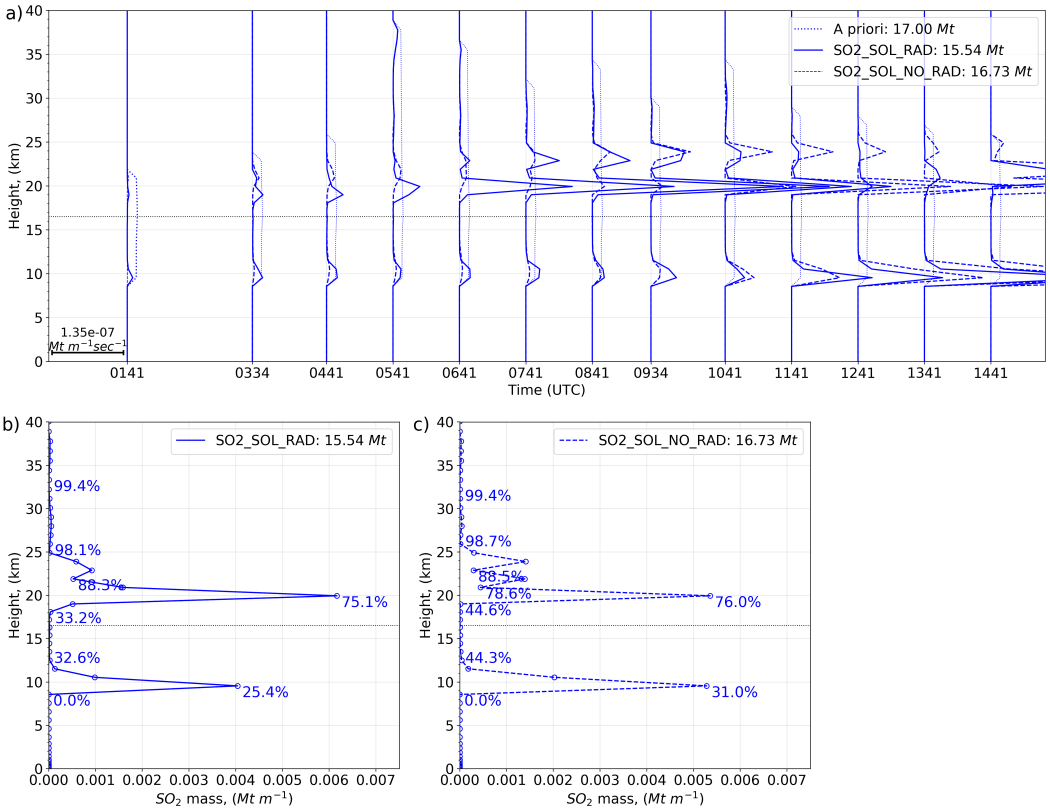

Figure 6. A posteriori SO_2 emission profiles ($Mt\ m^{-1}s^{-1}$): a) profiles used in the SO2_SOL_RAD (solid line) and SO2_SOL_NO_RAD (dashed line) runs. A priori emission profile – dotted line. Corresponding time-integrated SO_2 emission profiles ($Mt\ m^{-1}$) from the b) SO2_SOL_RAD and c) SO2_SOL_NO_RAD runs. Percentage numbers on plots b) and c) denote vertically integrated from bottom to top SO_2 emission mass. The dotted horizontal line marks the tropopause.

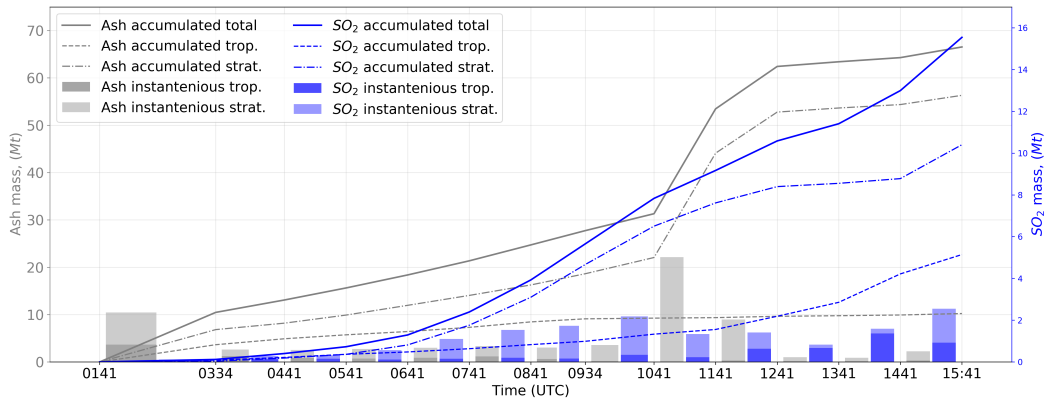

Figure 7. Atmospheric partitioning and evolution of the ash and SO_2 emissions based on a posteriori profiles used in the SO2_SOL_RAD run. The height of the bin exhibits the erupted mass integrated over the specific time interval (Mt). The lines mark the mass accumulation over time (Mt). Solid lines correspond to the total (stratospheric and tropospheric) mass, whereas dashed (tropospheric) and dotted-dashed (stratospheric) lines represent individual components. Ash is presented in gray, and SO_2 is marked in blue.

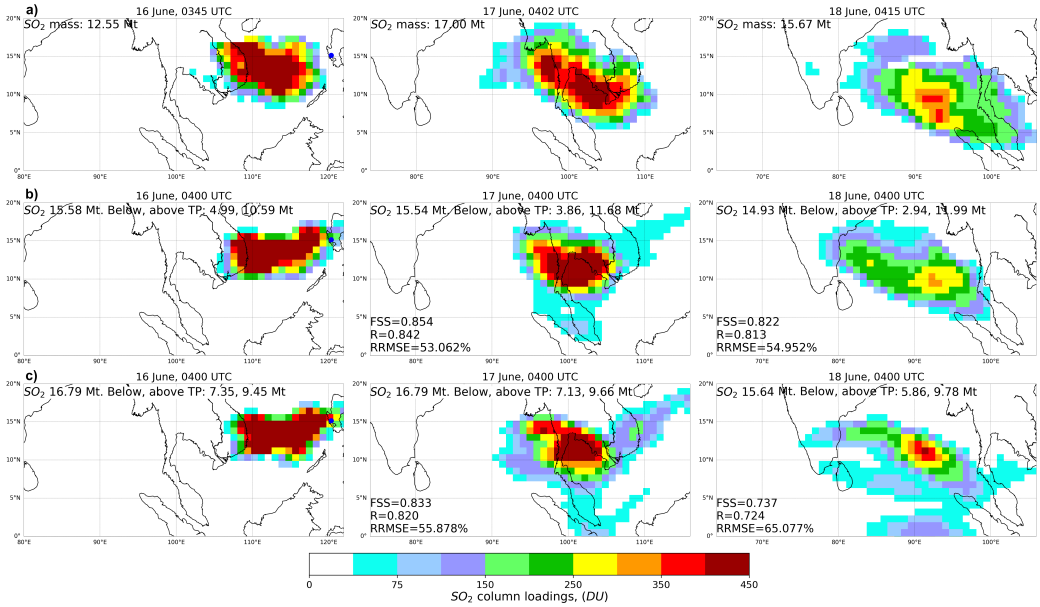

Figure 8. Observed and simulated SO_2 column loadings, (DU): a) TOMS retrievals on 0345 UTC 16 June, 0402 UTC 17 June, and 0415 UTC 18 June. Simulated SO_2 columns loadings at 0400 UTC on 16, 17, and 18 June from the b) SO2_SOL_RAD and c) SO2_SOL_NO_RAD runs.

3.3 Vertical Characteristics of Ash and SO_2 Clouds

Latitude-averaged (5°–15°N) vertical cross sections of ash and SO_2 concentrations in the SO2_SOL_RAD and SO2_SOL_NO_RAD runs on 16, 17, and 18 June (at 0400 UTC) are presented in Fig. 9. In the SO2_SOL_RAD run, the core of the ash cloud stays below TP on 16 June, but on 18 June, it lofts due to ash heating at 18 km evolving the SO_2 into the stratosphere. The secondary maximum of the ash concentration is centered between 23 and 28 km on 16 June. The clouds of ash and SO_2 overlap. Some part of the SO_2 cloud reaches 35 km at 0400 UTC on 16 June. The core of the SO_2 cloud rises by 1 km per day starting at 19 km on 16 June. On 18 June, it reaches 21.5 km. In the SO2_SOL_NO_RAD run, the ash and SO_2 clouds do not climb. At 0400 UTC on 18 June, the ash cloud almost dissipated in the SO2_SOL_NO_RAD experiment.

The height of the center of the mass, z_c of the ash columns in the SO2_SOL_RAD and SO2_SOL_NO_RAD runs at 0400 UTC on 16, 17, and 18 June are presented in Fig. 10. The height of the center of mass of ash and SO_2 clouds was calculated using the following formula:

$$z_c(x,y,t) = \frac{\int_{z_s}^{z_{top}} z\ q(x,y,z,t)\,dz}{\int_{z_s}^{z_{top}} q(x,y,z,t)\,dz}, \tag{7}$$

where q denotes the concentration of ash or SO_2, z_s and z_{top} represent the surface elevation and altitude at the top of the atmosphere (TOA), respectively, and y and x are the latitude and longitude. In the SO2_SOL_RAD run, on 16 June, the significant northern part of the ash cloud is in the stratosphere (≈18 to 25 km), whereas the southern part is in the troposphere (≈14 to 17 km). Ash ejected above 20 km moves westward, but the ash in the troposphere moves southward. On 17 June, the northern part of the center of mass of the ash cloud descends to ≈17 to 21 km and the top of the southern part to ≈14 to 15 km. This descent is due to the gravitational settling of ash particles. On 18 June, the tropospheric ash is likely washed out, and the southern part of the cloud

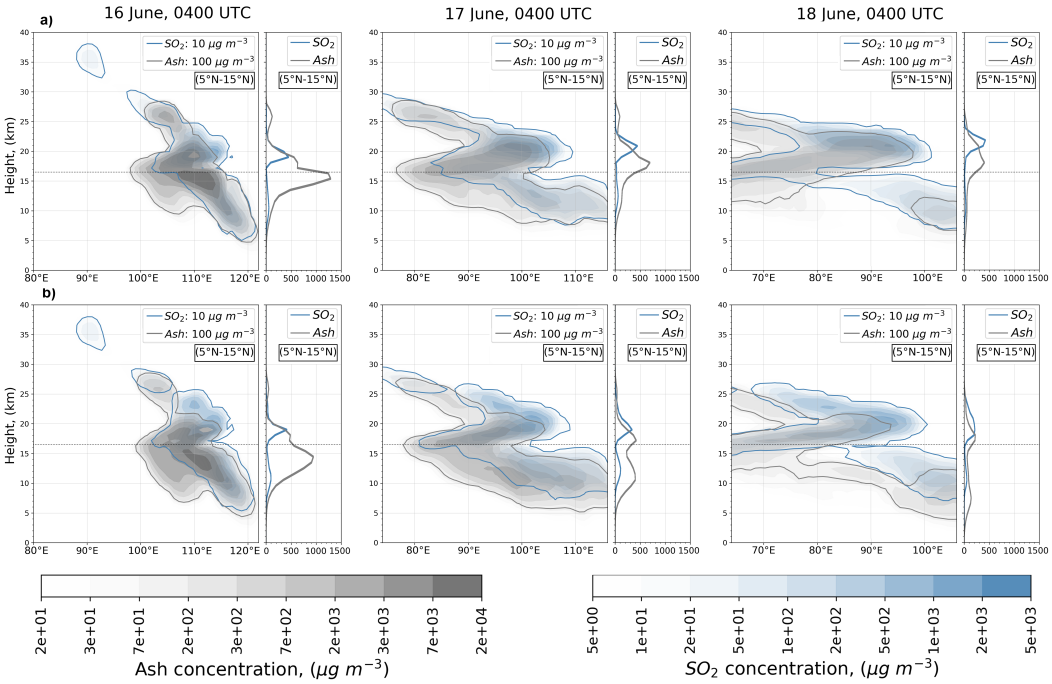

Figure 9. Latitude-averaged (5°–15°N) cross sections of the ash and SO_2 mass concentrations (μg m^{-3}) obtained at 0400 UTC on 16, 17, and 18 June from the a) SO2_SOL_RAD and b) SO2_SOL_NO_RAD runs. The dotted horizontal line marks the tropopause.

disappears, but the northern part stays above the TP. In the SO2_SOL_NO_RAD run, the centers of mass of ash clouds are primarily below 17 km on 16 June, and the entire cloud disappears by 18 June.

The heights of the center of mass of SO_2 clouds in the SO2_SOL_RAD and SO2_SOL_NO_RAD runs at 0400 UTC on 16,17, and 18 June are presented in Fig. 11. In the SO2_SOL_RAD run on 16 June, the center of mass of the SO_2 cloud spans vertically up to 23 km (see Fig. 11a). The western part of the cloud is in the stratosphere at 17 to 23 km, whereas the eastern cloud part is primarily in the troposphere. This topography is similar to that of the ash cloud (see Fig. 10) because, in both cases, the stratospheric volcanic emissions are transported westward, but tropospheric emissions are transported southward. On 18 June, the major part of the cloud reaches 20 to 22 km, whereas the eastern part of the cloud remains between 16 and 20 km.

Hatching marks the areas where the center of mass of the SO_2 cloud is below the center of mass of the ash cloud. In these areas, the TOMS can observe only the upper portion of the SO_2 cloud and underestimates the SO_2 column mass. However, these areas are limited. In the SO2_SOL_NO_RAD run, the center of mass of the SO_2 cloud remains above the center of the mass of the ash cloud on 16–18 June.

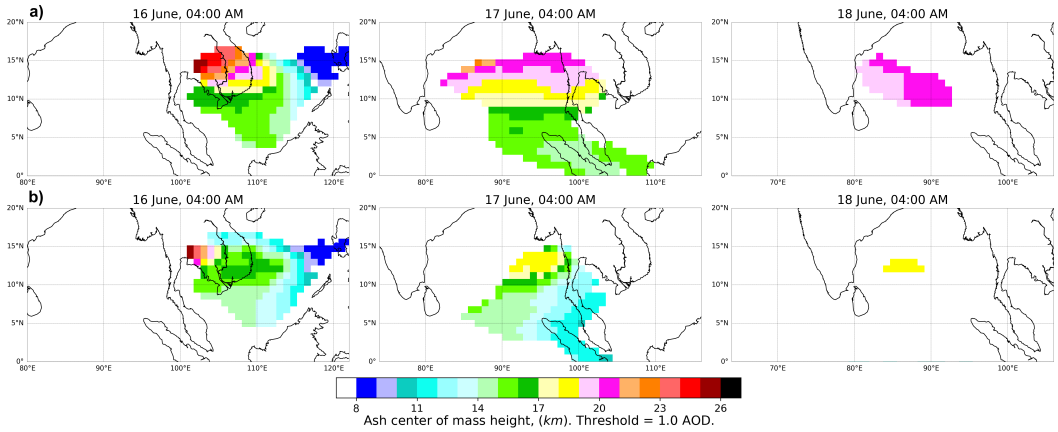

Figure 10. Simulated height of the center of mass of the ash cloud at 0400 UTC on 16, 17, and 18 June from the a) SO2_SOL_RAD and b) SO2_SOL_NO_RAD runs.

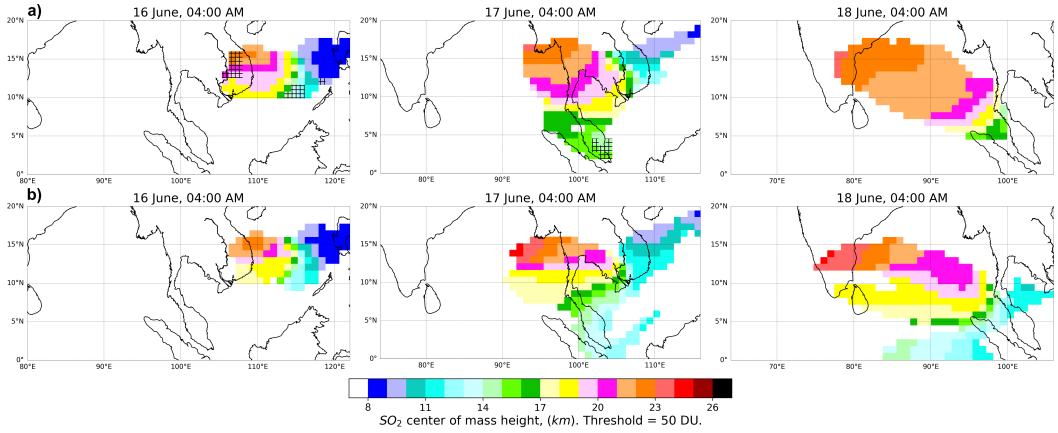

Figure 11. Simulated height of the center of mass of the SO_2 cloud at 0400 UTC on 16, 17, and 18 June from the a) SO2_SOL_RAD and b) SO2_SOL_NO_RAD runs. Hatched cells mark areas where the center of mass of the ash cloud is higher than the center of mass of the SO_2 cloud.

3.4 Long-term Volcanic Cloud Evolution

To evaluate the performance of the inversion, we conducted a three-month simulation using 3D distributions of ash and SO_2 obtained from the SO2_SOL_RAD run at 0400 UTC on 16 June. These distributions are used as initial conditions for the SOL_RAD run. We assessed this run against observations and compared it with the CW17S111A10 run (see Table 1) from Stenchikov et al. (2021). Both runs were conducted in the latitude belt domain (see Fig. 3), and both runs have approximately the same amount of fine ash and SO_2, but the vertical distributions of emissions are different. The CW17S111A10 run in Stenchikov et al. (2021) starts at 0000 UTC on 15 June. Ash and SO_2 in this run are injected in a given volume centered at an altitude of 17 km with a constant mass emission rate for 24 h. The SOL_RAD run starts at 0400 UTC on 16 June.

Figure 12a-d compares the long-term evolution of the AOD at 1.00 μm computed in the SOL_RAD and CW17S111A10 runs with the SAGE observations (L. Thomason & Peter, 2006). SAGE is a limb-viewing instrument that measures aerosol extinction in the stratosphere at different altitudes. The original SAGE observations have multiple gaps. L. Thomason and Peter (2006) filled these gaps using various techniques. We further refer to this dataset as SAGE/ASAP. For the SOL_RAD run, we present the whole column AOD and stratospheric AOD (see Fig. 12b,c), respectively. The SOL_RAD AOD and CW17S111A10 AODs in Fig. 12b,c,d shifted slightly north compared with the SAGE/ASAP AOD. The maximum SAGE/ASAP AOD is in the 10°S–0° latitude belt, whereas the AOD maximum is in the northern hemisphere (0°–10°N) in both runs. The SOL_RAD AOD develops faster than the SAGE/ASAP and CW17S111A10 AODs because the initial SO_2 distribution has a significant tropospheric component that quickly converts to sulfate aerosols, enhancing the AOD. In the CW17S111A10 run, the tropospheric SO_2 emissions are only marginal, and SAGE does not detect tropospheric aerosols because of the clouds and other obstacles.

Figure 12e illustrates the averaged over the 30°S–60°N latitude belt SO_4 concentrations as a function of the height and time in the SOL_RAD and CW17S111A10 experiments. The time evolution of the sulfate aerosol clouds is similar in both runs; however, in the SOL_RAD, a significant tropospheric plume is visible for more than a month.

Figure 12f compares the time evolution of the SOL_RAD and CW17S111A10 AODs at 1.0 μm averaged over the tropical (20°S–20°N) latitude belt with the SAGE/ASAP AOD at 1.020 μm. Along with the simulated total AODs, we present the stratospheric and tropospheric AODs from both runs. The tropospheric AOD in the SOL_RAD experiment reaches 0.03 within two weeks after the eruption. It is almost half of the total AOD. It is larger than the SAGE/ASAP and CW17S111A10 AODs during the first month after the eruption. However, in the long run, the SOL_RAD stratospheric AOD compares well with the SAGE/ASAP and CW17S111A10 AOD.

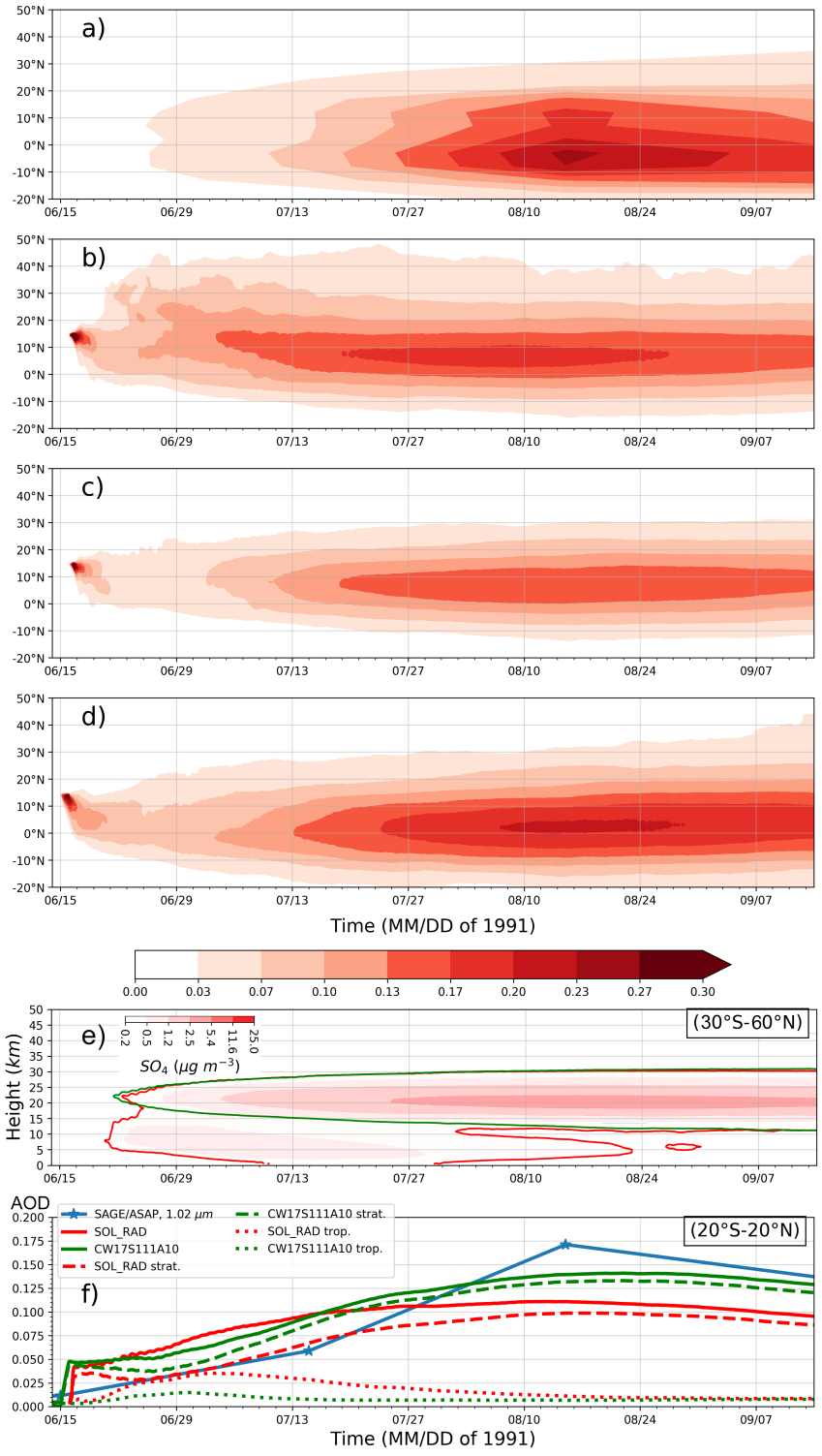

Figure 12. Observed and simulated aerosol diagnostics. a–d) Hovmöller diagrams of the zonal mean AOD: a) the SAGE/ASAP AOD at 1.020 μm (largely stratospheric), b) simulated column (stratospheric and tropospheric) AOD at 1.0 μm from SOL_RAD run, c) same as b) but with the stratospheric part only, d) simulated column from CW17S111A10 run, e) Hovmöller diagram of SO_4 concentration (μg m^{-3}) averaged over the 30°S–60°N latitude belt. The solid red contour line and red shading correspond to the SOL_RAD run. The green contour line corresponds to the CW17S111A10 run. f) Total (ash + sulfate aerosols) AOD averaged over the 20°S–20°N latitude belt obtained from the SOL_RAD (red lines) and CW17S111A10 (green lines) runs, the SAGE AOD at 1.020 μm (blue line with markers). The AOD partitioning into tropospheric and stratospheric components is indicated by dotted and dashed lines, respectively.

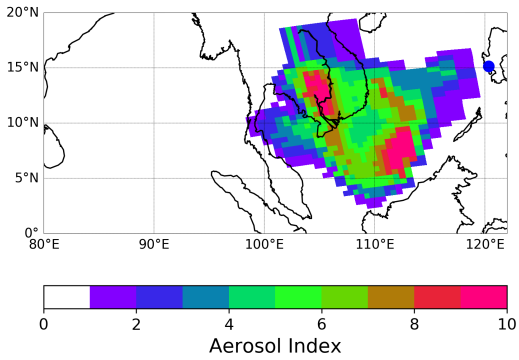

Figure 13. Simulated Aerosol Index on 16 June at 0400 UTC.

4 Aerosol Index

The ultraviolet (UV) AI quantifies the spectral contrast in radiances induced by particulate matter at the TOA. The slope of the spectral optical properties is inherently linked with the ability of aerosols to absorb and scatter radiation in UV light, deducing the aerosol origin from the sign of the AI. In the volcanic case, ash is conventionally associated with a positive AI (absorbing AI). Water, ice, and sulfate particles are associated with a negative AI (scattering AI) (Seftor et al., 1997; Krotkov et al., 1999; Rose et al., 2003).

Here, we validate our assumption on the linear relationship between the AI and ash loading by comparing the simulated AI distribution with TOMS AI retrieval (see Fig. 1a). The AI calculations follow a conventional physical approach, where we derive the atmospheric optical properties and make accurate radiative transfer calculations. Figure 13 demonstrates the simulated AI based on the ash distribution taken from the ASH_SOL_RAD run at 0400 UTC on 16 June. The comparison with the TOMS AI (see Fig. 1a) confirms that the assumption of the linear relation of the AI and ash column loadings (see Fig. 5a,b) works well at relatively low AOD values (see Fig. 5d). A description of the procedure for the AI calculation is presented in the Supplementary Material B1.

5 Discussion

Simulation results indicate that 66.53 Mt of fine ash and 15.54 of SO_2 were emitted during the climactic phase of the Mt. Pinatubo eruption. Nearly 77% of the ash mass was ejected between 12 and 23 km with the sharp maximum at 15 km. We estimated that ≈56% of ash was emitted below the TP. About ≈65% of the SO_2 mass was primarily distributed between 18 and 25 km with the maximum at ≈20 km. We found that 33% of the SO_2 emissions were below the TP. The inverse modeling places the SO_2 peak injection at 20 km, which is 3 km higher than in (Stenchikov et al., 2021). However, in the course of the sensitivity study, Stenchikov et al. (2021) found that releasing the eruptive materials at 20 km does not significantly change the evolution of the volcanic cloud in comparison with the 17 km injections. Most likely, this similarity is caused by small vertical wind shear in the layer above the tropopause. The inverted SO_2 distributions display a wider vertical spread of volcanic materials than was assumed in (Stenchikov et al., 2021).

SO_2 in the stratosphere oxidizes slowly with a characteristic time of 10 to 30 days, forming a long-lived sulfate aerosol that affects the climate. The tropospheric SO_2 mixes and oxidizes within a week, producing sulfate aerosols that remain in the troposphere

for a month. Moreover, SAGE does not observe tropospheric sulfate aerosols because of the clouds, which is another reason, along with sensor saturation, that it could underestimate the total column AOD. The previous simulations did not eject much of the SO_2 in the troposphere, assuming that all SO_2 estimated by the TOMS was injected in the stratosphere. Our results suggest that the stratosphere receives 67% of the injected SO_2 mass. Assuming that the total mass of SO_2 was ≈17 Mt, only ≈11 Mt of the SO_2 were converted into stratospheric sulfate aerosols that caused climatic perturbation. This estimate agrees with some model simulations, suggesting that a 10 - 12 Mt of SO_2 is sufficient to produce the observed climatic effects (Mills et al., 2016; Clyne et al., 2021).

The initial clouds of ash and SO_2 have a complex topography. The northern part of the ash and western part of the SO_2 clouds are higher than the corresponding southern and eastern parts of the clouds. Eruptive materials injected in the stratosphere are transported westward, but the volcanic material injected below the TP is transported southward. Ash predominantly has a lower altitude than the SO_2 and could not significantly shadow the SO_2 from the nadir viewing instruments, such as the TOMS.

We quantified the effect of ash radiative heating on the vertical distribution of volcanic ash emissions. In particular, accounting for ash radiative feedback tends to decrease the altitude of ash injections (i.e., the altitude of the maximum ash emissions is lower by 1.5 km when radiative feedback is enabled). It is in agreement with Stenchikov et al. (2021), where a vertical lofting of 1 km/day was reported. The inversion of SO_2 appears to be also sensitive to ash radiative heating. Due to ash radiative heating and plume lofting, the amount of SO_2 emitted above tropopause is ≈12% less in the run with radiative feedback compared to the run without radiative feedback. The amount of SO_2 in the stratosphere grows more rapidly during the 16-18 June period, i.e., 1.4 Mt when the radiative feedback is enabled and 0.3 Mt when it is disabled. The statistical scores calculated for the runs with ash radiative feedback are better than those without ash radiative feedback. The same amount of ash injected at higher altitudes will cause more significant heating and lofting because of lower air density. The radiative feedback is stronger for large eruptions as they can produce a higher initial ash concentration, causing stronger local radiative heating than small eruptions. However, the Raikoke eruption in 2019, which emitted an order of magnitude less ash and SO_2 than Pinatubo, exhibits a strong lofting of volcanic cloud because of unusually high absorptivity of ash (Khaykin et al., 2022).

Long-term calculations provide an additional constraint on the spatial-temporal evolution of the volcanic sulfate cloud. We calculated the three-month volcanic cloud's evolution using our inverted solutions as initial conditions for ash and SO_2. The spatial-temporal evolution of the simulated AOD agrees with the SAGE/ASAP dataset a month after the eruption. The first month in the simulation is affected by the SO_2 emissions in the troposphere that quickly oxidized, producing averaged over the tropical belt AOD on the order of 0.03. The simulated stratospheric AOD agrees with the SAGE/ASAP from the beginning of the simulation. The effect of the tropospheric SO_2 emissions was not recognized previously and has to be accounted for in evaluating the total SO_2 emission and in sulfate production during the initial stage of the volcanic cloud evolution. Some portion of quickly developed tropospheric sulfate could be lofted into the stratosphere, explaining the presence of sulfate aerosols in the volcanic cloud soon after the eruption (Guo, Rose, et al., 2004; Guo, Bluth, et al., 2004).

6 Conclusion

Volcanic eruptions produce a wide range of effects on the Earth's system. The initial placement of the volcanic material in the atmosphere, formed shortly after an eruption, governs the magnitude and duration of the corresponding climatic and photochemical effects via the evolution of the volcanic cloud.

In this study, we conducted inverse and forward modeling of the 1991 Mt. Pinatubo eruption. We derived the emission rates and profiles of ash and SO_2, simulated the evolution of the volcanic cloud, and compared the modeling results with the SAGE/ASAP observations and TOMS retrievals.

For the forward modeling, we used the regional meteorology-chemistry transport (WRF-Chem) model that explicitly calculates ash radiative feedback, atmospheric chemistry, and aerosol microphysics. To our knowledge, all previous inverse studies used dispersion models that did not account for the aerosol radiative feedback.

The SO_2 column loading, AI, and observed plume height were used to constrain the inverse modeling. We assumed that the ash loading is proportional to AI, which applies to a relatively low ash optical depth. The radiative transfer calculations further support this assumption because the modeled AI distribution compares well with the TOMS AI retrieval.

Ash radiative heating is a prominent lofting mechanism during the first few post-eruption days. At the same time, SO_2 and sulfate aerosols' radiative effects are weak. This allows us to use a sequential approach for inverse modeling. We first determine the solution for ash emissions and then use it to calculate the SO_2 emissions. The non-linearity associated with radiative heating and dynamic lofting is handled by imposing iterations using the emissions of optically active ash from the previous iteration.

The inverse modeling provides the emission profiles and distributions of ash and SO_2 on 16, 17, and 18 June, consistent with the TOMS AI and SO_2 loading retrievals. We also provide 3D distributions of the ash and SO_2 at 0400 UTC on 16 June, which can be used in long-term climate model simulations.

Since 1991 the observational network has evolved to include instruments that allow mapping the vertical distributions of volcanic ash, such as satellite-borne lidars e.g., Cloud-Aerosol Lidar with Orthogonal Polarization (CALIOP) (Winker et al., 2010). More advanced SO_2 retrievals have emerged from hyperspectral sensors such as the Ozone Monitoring Instrument (OMI) (Li et al., 2013), Ozone Mapping and Profiling Suite (OMPS) (Li et al., 2017), and TROPOspheric Monitoring Instrument (TROPOMI) (Theys et al., 2017). These instruments make measurements at hundreds of wavelengths in the UV that can be used to better separate the spectral signals from SO_2 absorption and those from other interfering processes, leading to reduced artifacts and noise in SO_2 retrievals. The hyperspectral measurements also help to partially mitigate signal saturation for dense SO_2 plumes, although interferences from volcanic ash and other aerosols remain a challenge. These instruments also offer higher spatial resolution than TOMS. For instance, TROPOMI retrieves SO_2 total column loadings at a spatial resolution of up to 3.5×5.5 km at the nadir. These observations, in combination with the methodology developed in this study, would allow a more detailed reconstruction of the initial distributions of volcanic materials that it was possible for the volcanic eruption occurred in the previous century.

7 Data Availability Statement

The inverted ash and SO_2 emission profiles and 3D distributions of ash and SO_2 at 0400 UTC on 16 June are provided at Ukhov and Stenchikov (2023).

Appendix A Metrics

A1 *FSS*

The FSS compares the observed values with the modeled values:

$$FSS = 1 - \frac{FBS}{FBS_{ref}}, \tag{A1}$$

where FBS is the fraction Brier score given by

$$FBS = \frac{1}{m}\sum_{k=1}^{m}\Big(O_k - M_k\Big)^2, \tag{A2}$$

where M_k is the modeled value, O_k is the retrieved value, m is the number of grid cells in the domain, and FBS_{ref} is given by

$$FBS_{ref} = \frac{1}{m}\Big(\sum_{k=1}^{m}O_k^2 + \sum_{k=1}^{m}M_k^2\Big). \tag{A3}$$

If FSS equals 1, it indicates a perfect agreement between the model and retrieval. Correspondingly, there is no match if the value of FSS is close to 0.

A2 R

The Pearson correlation coefficient R is given by

$$R = \frac{\sum_{k=1}^{m}\Big(M_k - \bar{M}\Big)\Big(O_k - \bar{O}\Big)}{\sqrt{\sum_{k=1}^{m}\Big(M_k - \bar{M}\Big)^2\sum_{k=1}^{m}\Big(O_k - \bar{O}\Big)^2}}, \tag{A4}$$

where

$$\bar{O} = \frac{1}{m}\sum_{k=1}^{m}O_k, \bar{M} = \frac{1}{m}\sum_{k=1}^{m}M_k, \tag{A5}$$

Moreover, R equals 1 if the horizontal distribution of the modeled and retrieved clouds of ash or SO_2 perfectly matches. If there is no match between the model and retrieval, R is close to 0.

A3 RRMSE

The relative root mean squared error $RRMSE$ is defined by

$$RRMSE = \frac{\sqrt{\sum_{k=1}^{m}\Big(O_k - M_k\Big)^2}}{\sqrt{\sum_{k=1}^{m}O_k^2}}. \tag{A6}$$

Appendix B Supplementary Information

B1 Radiance Simulator

We developed a radiance simulator to calculate the AI and compare it with the TOMS AI retrieval. The modeling framework was previously employed in (Mok et al., 2016; Osipov et al., 2020) and described in detail in Appendix A (Osipov et al., 2020). This section outlines the modeling setup adjustments necessary to simulate the radiances, as observed by the TOMS instrument. We consider the position and viewing geometry of the

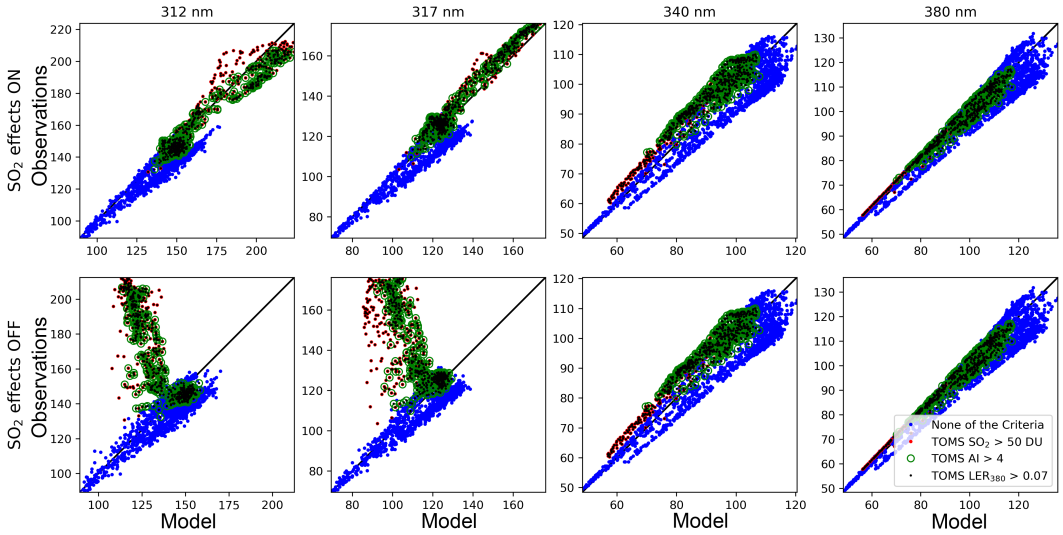

Figure B1. Comparison of the simulated and observed N values at four TOMS channels. Synthetic N values are based on the optimal WRF-Chem solution coupled to the line-by-line (LBLRTM) and radiative transfer (DISORT) calculations. Simulated N values account for the optical properties of the SO_2 in the top row and exclude them in the bottom row. The comparison is restricted to the TOMS overpass over the Pinatubo plume on 16 June. Larger N values correspond to the smaller upwelling radiances and indicate a stronger extinction (absorption).

sounder, the effects of the relevant trace gases (including O_3 and enhanced SO_2 loadings) and aerosols, and the instrument-specific settings (e.g., the slit function and exact wavelengths of the six TOMS channels).

The greenhouse gas SO_2 absorbs strongly in UV light, affecting the first two TOMS channels (312 and 317 nm). We included the SO_2 effects on radiative transfer and employed the optimal inverse modeling solution (WRF-Chem simulation) to prescribe the spatial and vertical distribution of SO_2. We scaled the O_3 and SO_2 column loading to match those in the TOMS retrievals to allow a meaningful comparison with remote sensing products. Figure B1 (top row) indicates that the simulator captures the radiances (N values) across the entire range of the SO_2 loadings, confirming the model skill.

We treated the surface albedo as Lambertian and prescribed a spectrally gray surface albedo based on the TOMS Lambert-equivalent reflectivity (LER) at 380 nm (LER380). By incorporating the TOMS LER, we included the effects of the clouds in a manner consistent with the TOMS retrieval algorithm.

We calculated the AI using the ash profile and mass concentrations computed in the ASH_SOL_RAD run. We derived the optical properties of aerosols and carried out radiative transfer calculations. We followed the definition of the AI as provided in Equation 1 in Torres et al. (1998) and Vries et al. (2009). The complex refractive index of ash in UV is 1.55+i0.0004.

We configured the latest version of DISORT (v4.0.99) (Osipov, 2023) to use 16 streams to conduct radiative transfer calculations and 64 moments to represent the phase function. We applied the DeltaM+ plus correction. The elevated aerosol layer significantly perturbs the background optical properties and represents a numerically challenging case to obtain accurate TOA radiances. The pseudo-spherical correction in DISORT drastically improves the numerical stability of the solutions.

Author contribution A.U. conducted the simulations and drafted the manuscript. S.O. conducted the radiative transfer and AI calculations. G.S. analyzed the results. O.D., A.L., N.G., C.L., and N.K. contributed to the analysis.

Competing Interests The authors declare that they have no conflicts of interest.

Acknowledgments
The research reported in this publication was supported by funding from the King Abdullah University of Science and Technology (KAUST). For computer time, this research used the resources of the Supercomputing Laboratory at KAUST.

References

Abdelkader, M., Stenchikov, G., Pozzer, A., Tost, H., & Lelieveld, J. (2022). The effect of ash, water vapor, and heterogeneous chemistry on the evolution of a pinatubo-size volcanic cloud. *Atmospheric Chemistry and Physics Discussions*, *2022*, 1–49. Retrieved from `https://acp.copernicus.org/preprints/acp-2022-177/` doi: 10.5194/acp-2022-177

Aquila, V., Oman, L. D., Stolarski, R. S., Colarco, P. R., & Newman, P. A. (2012). Dispersion of the volcanic sulfate cloud from a mount pinatubo–like eruption. *Journal of Geophysical Research: Atmospheres*, *117*(D6).

Bluth, G. J., Doiron, S. D., Schnetzler, C. C., Krueger, A. J., & Walter, L. S. (1992). Global tracking of the so2 clouds from the june, 1991 mount pinatubo eruptions. *Geophysical Research Letters*, *19*(2), 151–154.

Brühl, C., Schallock, J., Klingmüller, K., Robert, C., Bingen, C., Clarisse, L., ... Rieger, L. (2018). Stratospheric aerosol radiative forcing simulated by the chemistry climate model emac using aerosol cci satellite data. *Atmospheric Chemistry and Physics*, *18*(17), 12845–12857.

Carn, S., & Krotkov, N. (2016). Ultraviolet satellite measurements of volcanic ash. In *Volcanic ash* (pp. 217–231). Elsevier.

Carn, S. A., Krueger, A. J., Krotkov, N. A., Yang, K., & Evans, K. (2009). Tracking volcanic sulfur dioxide clouds for aviation hazard mitigation. *Natural Hazards*, *51*(2), 325–343.

Chin, M., Ginoux, P., Kinne, S., Torres, O., Holben, B. N., Duncan, B. N., ... Nakajima, T. (2002). Tropospheric aerosol optical thickness from the gocart model and comparisons with satellite and sun photometer measurements. *Journal of the atmospheric sciences*, *59*(3), 461–483.

Clyne, M., Lamarque, J.-F., Mills, M. J., Khodri, M., Ball, W., Bekki, S., ... others (2021). Model physics and chemistry causing intermodel disagreement within the volmip-tambora interactive stratospheric aerosol ensemble. *Atmospheric Chemistry and Physics*, *21*(5), 3317–3343.

Dee, D. P., Uppala, S. M., Simmons, A., Berrisford, P., Poli, P., Kobayashi, S., ... others (2011). The era-interim reanalysis: Configuration and performance of the data assimilation system. *Quarterly Journal of the royal meteorological society*, *137*(656), 553–597.

Eckhardt, S., Prata, A., Seibert, P., Stebel, K., & Stohl, A. (2008). Estimation of the vertical profile of sulfur dioxide injection into the atmosphere by a volcanic eruption using satellite column measurements and inverse transport modeling. *Atmospheric Chemistry and Physics*, *8*(14), 3881–3897.

English, J. M., Toon, O. B., & Mills, M. J. (2013). Microphysical simulations of large volcanic eruptions: Pinatubo and toba. *Journal of Geophysical Research: Atmospheres*, *118*(4), 1880–1895.

Fero, J., Carey, S. N., & Merrill, J. T. (2009). Simulating the dispersal of tephra from the 1991 pinatubo eruption: Implications for the formation of widespread

ash layers. *Journal of Volcanology and Geothermal Research*, *186*(1-2), 120–131.

Fisher, B. L., Krotkov, N. A., Bhartia, P. K., Li, C., Carn, S. A., Hughes, E., & Leonard, P. J. (2019). A new discrete wavelength backscattered ultraviolet algorithm for consistent volcanic so 2 retrievals from multiple satellite missions. *Atmospheric Measurement Techniques*, *12*(9), 5137–5153.

Grell, G. A., Peckham, S. E., Schmitz, R., McKeen, S. A., Frost, G., Skamarock, W. C., & Eder, B. (2005). Fully coupled "online" chemistry within the wrf model. *Atmospheric Environment*, *39*(37), 6957–6975.

Guo, S., Bluth, G. J., Rose, W. I., Watson, I. M., & Prata, A. (2004). Re-evaluation of so2 release of the 15 june 1991 pinatubo eruption using ultraviolet and infrared satellite sensors. *Geochemistry, Geophysics, Geosystems*, *5*(4).

Guo, S., Rose, W. I., Bluth, G. J., & Watson, I. M. (2004). Particles in the great pinatubo volcanic cloud of june 1991: The role of ice. *Geochemistry, Geophysics, Geosystems*, *5*(5).

Herman, J., Bhartia, P., Torres, O., Hsu, C., Seftor, C., & Celarier, E. (1997). Global distribution of uv-absorbing aerosols from nimbus 7/toms data. *Journal of Geophysical Research: Atmospheres*, *102*(D14), 16911–16922.

Holasek, R., Self, S., & Woods, A. (1996). Satellite observations and interpretation of the 1991 mount pinatubo eruption plumes. *Journal of Geophysical Research: Solid Earth*, *101*(B12), 27635–27655.

Khaykin, S. M., De Laat, A. J., Godin-Beekmann, S., Hauchecorne, A., & Ratynski, M. (2022). Unexpected self-lofting and dynamical confinement of volcanic plumes: the raikoke 2019 case. *Scientific Reports*, *12*(1), 22409.

Kristiansen, N., Stohl, A., Prata, A., Richter, A., Eckhardt, S., Seibert, P., ... others (2010). Remote sensing and inverse transport modeling of the kasatochi eruption sulfur dioxide cloud. *Journal of Geophysical Research: Atmospheres*, *115*(D2).

Krotkov, N., Krueger, A., & Bhartia, P. (1997). Ultraviolet optical model of volcanic clouds for remote sensing of ash and sulfur dioxide. *Journal of Geophysical Research: Atmospheres*, *102*(D18), 21891–21904.

Krotkov, N., Pawan, K., Bradford, F., & Peter, L. (2019). Toms/n7 ms so2 vertical column 1-orbit l2 swath 50x50 km v3. *Greenbelt, MD, USA, Goddard Earth Sciences Data and Information Services Center (GES DISC) [Dataset]*. doi: 10.5067/MEASURES/SO2/DATA204

Krotkov, N., Torres, O., Seftor, C., Krueger, A., Kostinski, A., Rose, W. I., ... Schaefer, S. (1999). Comparison of toms and avhrr volcanic ash retrievals from the august 1992 eruption of mt. spurr. *Geophysical research letters*, *26*(4), 455–458.

Krueger, A., Walter, L., Bhartia, P., Schnetzler, C., Krotkov, N., Sprod, I. t., & Bluth, G. (1995). Volcanic sulfur dioxide measurements from the total ozone mapping spectrometer instruments. *Journal of Geophysical Research: Atmospheres*, *100*(D7), 14057–14076.

Krueger, A. J. (1983). Sighting of el chichon sulfur dioxide clouds with the nimbus 7 total ozone mapping spectrometer. *Science*, *220*(4604), 1377–1379.

Li, C., Joiner, J., Krotkov, N. A., & Bhartia, P. K. (2013). A fast and sensitive new satellite so2 retrieval algorithm based on principal component analysis: Application to the ozone monitoring instrument. *Geophysical Research Letters*, *40*(23), 6314–6318.

Li, C., Krotkov, N., Zhang, Y., Leonard, P., & Joiner, J. (2017). Omps/npp pca so2 total column 1-orbit l2 swath 50× 50 km v1. *Goddard Earth Sciences Data and Information Services Center (GES DISC): Greenbelt, MD, USA*.

Long, C. S., & Stowe, L. L. (1994). Using the noaa/avhrr to study stratospheric aerosol optical thicknesses following the mt. pinatubo eruption. *Geophysical research letters*, *21*(20), 2215–2218.

Madronich, S. (1987). Photodissociation in the atmosphere: 1. actinic flux and the effects of ground reflections and clouds. *Journal of Geophysical Research: Atmospheres*, *92*(D8), 9740–9752.

Miguez-Macho, G., Stenchikov, G. L., & Robock, A. (2004). Spectral nudging to eliminate the effects of domain position and geometry in regional climate model simulations. *Journal of Geophysical Research: Atmospheres*, *109*(D13).

Mills, M. J., Schmidt, A., Easter, R., Solomon, S., Kinnison, D. E., Ghan, S. J., ... others (2016). Global volcanic aerosol properties derived from emissions, 1990–2014, using cesm1 (waccm). *Journal of Geophysical Research: Atmospheres*, *121*(5), 2332–2348.

Mok, J., Krotkov, N. A., Arola, A., Torres, O., Jethva, H., Andrade, M., ... Ren, X. (2016, 11). Impacts of brown carbon from biomass burning on surface uv and ozone photochemistry in the amazon basin. *Scientific Reports 2016 6:1*, *6*, 1-9. Retrieved from `https://www.nature.com/articles/srep36940` doi: 10.1038/srep36940

Niemeier, U., Timmreck, C., Graf, H.-F., Kinne, S., Rast, S., & Self, S. (2009). Initial fate of fine ash and sulfur from large volcanic eruptions. *Atmospheric Chemistry and Physics*, *9*(22), 9043–9057.

Osipov, S. (2023). Disort matlab wrapper (1.0) [software]. Retrieved from `https://doi.org/10.5281/zenodo.7790058`

Osipov, S., Stenchikov, G., Tsigaridis, K., LeGrande, A. N., & Bauer, S. E. (2020). The role of the so radiative effect in sustaining the volcanic winter and soothing the toba impact on climate. *Journal of Geophysical Research: Atmospheres*, *125*(2), e2019JD031726.

Pollack, J. B., Toon, O. B., & Khare, B. N. (1973). Optical properties of some terrestrial rocks and glasses. *Icarus*, *19*(3), 372–389.

Prata, A., Carn, S., Stohl, A., & Kerkmann, J. (2007). Long range transport and fate of a stratospheric volcanic cloud from soufrière hills volcano, montserrat. *Atmospheric Chemistry and Physics*, *7*(19), 5093–5103.

Quaglia, I., Timmreck, C., Niemeier, U., Visioni, D., Pitari, G., Brodowsky, C., ... others (2023). Interactive stratospheric aerosol models' response to different amounts and altitudes of so 2 injection during the 1991 pinatubo eruption. *Atmospheric Chemistry and Physics*, *23*(2), 921–948.

Ramaswamy, V., Collins, W., Haywood, J., Lean, J., Mahowald, N., Myhre, G., ... others (2019). Radiative forcing of climate: the historical evolution of the radiative forcing concept, the forcing agents and their quantification, and applications. *Meteorological Monographs*, *59*, 14–1.

Roberts, N. M., & Lean, H. W. (2008). Scale-selective verification of rainfall accumulations from high-resolution forecasts of convective events. *Monthly Weather Review*, *136*(1), 78–97.

Robock, A. (2000). Volcanic eruptions and climate. *Reviews of geophysics*, *38*(2), 191–219.

Rose, W. I., Gu, Y., Watson, I., Yu, T., Bluth, G., Prata, A., ... others (2003). The february-march 2000 eruption of hekla, iceland from a satellite perspective. *Geophysical Monograph-american Geophysical Union*, *139*, 107–132.

Searcy, C., Dean, K., & Stringer, B. (1998). Puff: A volcanic ash tracking and prediction model. *Journal of Volcanology and Geothermal Research*, *80*, 1–16.

Seftor, C., Hsu, N., Herman, J., Bhartia, P., Torres, O., Rose, W. I., ... Krotkov, N. (1997). Detection of volcanic ash clouds from nimbus 7/total ozone mapping spectrometer. *Journal of Geophysical Research: Atmospheres*, *102*(D14), 16749–16759.

Seibert, P. (2000). Inverse modelling of sulfur emissions in europe based on trajectories. *Geophysical Monograph-american Geophysical Union*, *114*, 147–154.

Seibert, P., Kristiansen, N. I., Richter, A., Eckhardt, S., Prata, A. J., & Stohl, A. (2011). Uncertainties in the inverse modelling of sulphur dioxide eruption

profiles. *Geomatics, Natural Hazards and Risk*, *2*(3), 201–216.

Self, S., Zhao, J.-X., Holasek, R. E., Torres, R. C., & King, A. J. (1993). *The atmospheric impact of the 1991 mount pinatubo eruption* (Tech. Rep.).

Skamarock, W. C., Klemp, J. B., Dudhia, J., Gill, D. O., Barker, D. M., Wang, W., & Powers, J. G. (2005). *A description of the advanced research wrf version 2* (Tech. Rep.). National Center For Atmospheric Research Boulder Co Mesoscale and Microscale Meteorology Div.

Stenchikov, G. (2021). The role of volcanic activity in climate and global changes. In *Climate change* (pp. 607–643). Elsevier.

Stenchikov, G., Ukhov, A., Osipov, S., Ahmadov, R., Grell, G., Cady-Pereira, K., ... Iacono, M. (2021). How does a pinatubo-size volcanic cloud reach the middle stratosphere? *Journal of Geophysical Research: Atmospheres*, e2020JD033829.

Stockwell, W. R., Kirchner, F., Kuhn, M., & Seefeld, S. (1997). A new mechanism for regional atmospheric chemistry modeling. *Journal of Geophysical Research: Atmospheres*, *102*(D22), 25847–25879.

Stohl, A., Forster, C., Frank, A., Seibert, P., & Wotawa, G. (2005). The lagrangian particle dispersion model flexpart version 6.2. *Atmospheric Chemistry and Physics*, *5*(9), 2461–2474.

Stohl, A., Prata, A., Eckhardt, S., Clarisse, L., Durant, A., Henne, S., ... others (2011). Determination of time-and height-resolved volcanic ash emissions and their use for quantitative ash dispersion modeling: the 2010 eyjafjallajökull eruption. *Atmospheric Chemistry and Physics*, *11*(9), 4333–4351.

Stuefer, M., Freitas, S., Grell, G., Webley, P., Peckham, S., McKeen, S., & Egan, S. (2013). Inclusion of ash and so 2 emissions from volcanic eruptions in wrf-chem: development and some applications. *Geoscientific Model Development*, *6*(2), 457–468.

Stunder, B. J., Heffter, J. L., & Draxler, R. R. (2007). Airborne volcanic ash forecast area reliability. *Weather and Forecasting*, *22*(5), 1132–1139.

Suzuki, T., et al. (1983). A theoretical model for dispersion of tephra. *Arc volcanism: physics and tectonics*, *95*, 113.

Theys, N., De Smedt, I., Yu, H., Danckaert, T., van Gent, J., Hörmann, C., ... others (2017). Sulfur dioxide retrievals from tropomi onboard sentinel-5 precursor: algorithm theoretical basis. *Atmospheric Measurement Techniques*, *10*(1), 119–153.

Thomason, L., & Peter, T. (Eds.). (2006). *SPARC Assessment of Stratospheric Aerosol Properties (ASAP)* (Vol. No. 4; Tech. Rep.). SPARC [Dataset]. Retrieved from `https://www.sparc-climate.org/data-centre/data-access/assessment-of-stratospheric-aerosol-properties/`

Thomason, L. W. (1992). Observations of a new sage ii aerosol extinction mode following the eruption of mt. pinatubo. *Geophysical research letters*, *19*(21), 2179–2182.

Timmreck, C., Graf, H.-F., Zanchettin, D., Hagemann, S., Kleinen, T., & Krüger, K. (2012). Climate response to the toba super-eruption: Regional changes. *Quaternary International*, *258*, 30–44.

Torres, O., Bhartia, P., Herman, J., Ahmad, Z., & Gleason, J. (1998). Derivation of aerosol properties from satellite measurements of backscattered ultraviolet radiation: Theoretical basis. *Journal of Geophysical Research: Atmospheres*, *103*(D14), 17099–17110.

Ukhov, A., Ahmadov, R., Grell, G., & Stenchikov, G. (2021). Improving dust simulations in wrf-chem v4. 1.3 coupled with the gocart aerosol module. *Geoscientific Model Development*, *14*(1), 473–493.

Ukhov, A., & Stenchikov, G. (2023). Supplementary material for "inverse modeling of the initial stage of the 1991 pinatubo volcanic cloud accounting for radiative feedback of volcanic ash" paper [dataset]. Retrieved from `https://zenodo.org/record/7708158` doi: 10.5281/ZENODO.7708158

Vries, M. J. P. D., Beirle, S., & Wagner, T. (2009). Uv aerosol indices from sciamachy: Introducing the scattering index (sci). *Atmospheric Chemistry and Physics*, *9*, 9555-9567. doi: 10.5194/ACP-9-9555-2009

Winker, D., Pelon, J., Coakley Jr, J., Ackerman, S., Charlson, R., Colarco, P., ... others (2010). The calipso mission: A global 3d view of aerosols and clouds. *Bulletin of the American Meteorological Society*, *91*(9), 1211–1230.

Zhu, Y., Toon, O. B., Jensen, E. J., Bardeen, C. G., Mills, M. J., Tolbert, M. A., ... Woods, S. (2020). Persisting volcanic ash particles impact stratospheric so2 lifetime and aerosol optical properties. *Nature communications*, *11*(1), 1–11.